Electronic and elastic properties of CaF$_2$ under high pressure from *ab initio* calculations

Electronic and elastic properties of CaF$_2$ under high pressure from *ab initio* calculations

H Shi[1,2,3]**, W Luo**[1,2]**, B Johansson**[1,2] **and R Ahujia**[1,2]

[1] Department of Physics, Condensed Matter Theory Group, Uppsala University, Box 530, S-751 21 Uppsala, Sweden
[2] Applied Materials Physics, Department of Materials and Engineering, Royal Institute of Technology (KTH), S-100 44 Stockholm, Sweden
[3] Beijing Institute of Technology, Department of Physics, Beijing 100081, People's Republic of China

E-mail: Wei.luo@fysik.uu.se

Abstract
Calcium fluoride CaF$_2$ has been studied by using density functional theory (DFT) with the generalized gradient approximation (GGA). Our results demonstrate that the sequence of the pressure-induced structural transition of CaF$_2$ is the fluorite structure ($Fm\bar{3}m$), the orthorhombic cotunnite-type structure ($Pnma$), and the hexagonal Ni$_2$In-type structure ($P6_3/mmc$). The two transitions occur at pressures of 8 GPa and 105 GPa, accompanied by volume collapses of 8.4% and 1.2%, respectively. The energy band gap increases with pressure in the $Fm\bar{3}m$ and the forepart of $Pnma$ phases. However, on increasing the pressure beyond 60 GPa, the gap decreases, which is due to the fluorine p$_z$-states shifting toward the Fermi energy. In addition, the elastic properties versus pressure are also discussed. Our calculated elastic constants for the cubic phase at ambient pressure are in agreement with the experimental values. The stress–strain coefficient calculations show that shear transformations in the $Pnma$ phase are more difficult than in the cubic phase and the compressibility along the c_h (or a_o) direction for the orthorhombic phase is stronger than that in the hexagonal crystal.

(Some figures in this article are in colour only in the electronic version)

1. Introduction

Fluorite CaF$_2$ is a well-known face-centered-cubic (fcc) ionic crystal. Because of its excellent transmission properties without absorption bands over a wide wavelength range from UV to IR, CaF$_2$ has important optical applications, such as a candidate lens material for photolithography at wavelengths in the deep ultraviolet region. These optical properties are due to its structural and electronic properties, such as a very large band gap [1–5]. In addition, the knowledge of elastic properties is essential to interpret the thermodynamic and elastic dimensions of solids at high pressures or temperatures. The elasticity offers more information than the volume in interpreting the pressure or temperature dependence of the equation of state because the compressibility is defined by the derivative of volume. The elastic properties also provide a base

for examining the Earth's deep interior [6]. CaF$_2$ is one of the important compounds of broad interest in geoscience. Thus, the behaviors of its elastic properties under the influence of high pressure have attracted our attention.

Pressure-induced phase transitions of CaF$_2$ have been studied by many research groups [7–14]. In summary, CaF$_2$ undergoes a phase transition from the cubic fluorite structure to an orthorhombic cotunnite-type structure and further transforms to a hexagonal Ni$_2$In-type structure with increasing pressure. In the first report of CaF$_2$ variation with pressure in 1966, Seifert *et al* showed that the cubic-to-orthorhombic transformation occurs in the pressure range 8– 10 GPa [7]. Other groups using various methods, such as x-ray diffraction, Raman spectroscopy and theoretical calculations, have also demonstrated this transition [8, 9, 11–15]. Recently, the strain gauge technique in an ideal hydrostatic pressure

at room temperature has been used to investigate the initial stages of phase transformations in CaF_2, which indicates that the phase transition pressure is 8.01 ± 0.01 GPa [13]. The high pressure orthorhombic phase has been shown to still be stable up to 49 GPa at room temperature by x-ray diffraction and Raman spectroscopy [9, 11]. For the orthorhombic-to-hexagonal transition, Wu *et al* reported that the transition pressure is 72 GPa using a first-principles method [16]. Experimentally, Dorfman *et al* performed an angle-dispersive x-ray diffraction experiment to investigate the behavior of CaF_2 at extreme pressure, which indicated that this transition occurs at 84 GPa [17].

The electronic structure and elastic properties of CaF_2 have been recently calculated from first principles and published by several research groups. At the beginning of the 1990s, Catti *et al* performed an all-electron *ab initio* Hartree–Fock (HF) calculation for the band structure and elastic constants of CaF_2 [18]. Different theoretical calculations of CaF_2 bulk electronic, optical and elastic properties have been compared and discussed extensively [3–5, 12, 14, 19, 20]. However, according to our knowledge, only a few articles described the influence of pressure on the electronic and optical properties of CaF_2 [12, 14] and there is no report about the relation between elastic properties and pressure that has been published up to now.

The *ab initio* simulation technique is a reliable tool for investigating the electronic structure and elastic properties of materials under extreme conditions, such as high pressure and temperature [21]. By using first-principles calculations, one can go far beyond the pressure and temperature range achieved experimentally. In this paper, the pressure-induced structural phase transitions, electronic structures and elastic properties of CaF_2, as well as geometrical structures, have been studied using first-principles method.

2. Calculation methods

We have studied the structural stabilities and the electronic and elastic properties under high pressure in CaF_2 by performing first-principles calculations based on the DFT. *Ab initio* simulations were performed using the projector augmented-wave (PAW) method [22] as implemented in the Vienna *ab initio* simulation package (VASP) code [23, 24], and the GGA [25] was used to describe the electronic exchange–correlation effects. We have chosen the exchange–correlation functional proposed by Perdew *et al* in 1991 using the GGA denoted hereby PW91 [25, 26]. For Ca atoms, we have used PAW potentials with the following orbitals treated as valence states: $3s^2 3p^6 4s^2$ configuration ($r_{core} = 2.300$ au), where r_{core} is the core radius. The hard PAW potential for F atoms is used for calculations in this work. Seven valence electrons for each F atom ($2s^2 2p^5$, $r_{core} = 1.100$ au) were taken into account. The remaining core electrons together with the nuclei were described by pseudopotentials in the framework of the PAW method. The calculations were performed using a cutoff energy of 875 eV and sampling the Brillouin zone with fixed k ($6 \times 6 \times 6$ for the $Fm\bar{3}m$ and $Pnma$ phases, and $8 \times 8 \times 8$ for the $P6_3/mmc$ phase) points with 10, 27 and

50 irreducible k points in the $Fm\bar{3}m$, $Pnma$ and $P6_3/mmc$ phases, respectively.

The elastic constants determine the stiffness of a crystal against an externally applied strain. For small deformations we expect a quadratic dependence of the crystal energy E on the strain (Hooke's law). Expanding the internal energy $E(V, \boldsymbol{\varepsilon})$ of the crystal with respect to the strain tensor gives [27]

$$E(V, \{\varepsilon_{mn}\}) = E(V) + V \sum_{ij} T_{ij} \varepsilon_{ij}$$

$$+ \frac{V}{2} \sum_{ijkl} C_{ijkl} \varepsilon_{ij} \varepsilon_{kl} + \cdots, \qquad (1)$$

where $\boldsymbol{\varepsilon}$ is the strain tensor, and the stress tensor $\boldsymbol{T}$ is defined by

$$T_{ij} = \frac{1}{V} \left[\frac{\partial E(V, \{\varepsilon_{mn}\})}{\partial \varepsilon_{ij}} \right]_{\boldsymbol{\varepsilon}=0}, \qquad (2)$$

the second order adiabatic elastic constants are given by

$$C_{ijkl} = \frac{1}{V} \left[\frac{\partial^2 E(V, \{\varepsilon_{mn}\})}{\partial \varepsilon_{ij} \partial \varepsilon_{kl}} \right]_{\boldsymbol{\varepsilon}=0}, \qquad (3)$$

and V is the volume of the unstrained crystal. It is convenient to use Voigt notation which takes advantage of the symmetries of the tensors: $xx \to 1$, $yy \to 2$, $zz \to 3$, $yz \to 4$, $xz \to 5$ and $xy \to 6$. Using this notation equation (1) becomes

$$E(V, \{\varepsilon_i\}) = E(V) + V \sum_i T_i \varepsilon_i + \frac{V}{2} \sum_{ij} C_{ij} \varepsilon_i \varepsilon_j + \cdots, \quad (4)$$

with the strain tensor given by

$$\boldsymbol{\varepsilon} = \begin{pmatrix} \varepsilon_1 & \frac{1}{2}\varepsilon_6 & \frac{1}{2}\varepsilon_5 \\ \frac{1}{2}\varepsilon_6 & \varepsilon_2 & \frac{1}{2}\varepsilon_4 \\ \frac{1}{2}\varepsilon_5 & \frac{1}{2}\varepsilon_4 & \varepsilon_3 \end{pmatrix}. \qquad (5)$$

The zero-strain tensor at a certain pressure corresponds to the equilibrium state, which has the minimum total energy at this pressure. As we can see from tables 1–3, for a volume conserving distortion, the total energy is larger than that of the zero-strain case at a certain pressure, presenting a parabolic strain–energy curve. For non-conserving volume distortions, strain energies have an additional term which comes from the pressure effect.

To calculate the elastic constants from first principles, one first has to select a set of linearly independent distortions. Then for each of these distortions the total energy is calculated for a number of different distortion amplitudes, producing an energy parabola for each distortion. Since the potential energy (equation (4)) for each distortion can be expressed as a linear combination of elastic constants multiplied by the square of the distortion amplitude, the curvatures of the different energy parabolas together with their corresponding linear combination of elastic constants produce a set of linear equations. In solving these equations the elastic constants are finally extracted. Since the distortions are often applied around the equilibrium of the lattice the first summation in equation (4) is equal to zero. Furthermore we consider how the single-crystal elastic moduli change with pressure. Specifically, we

Table 1. Strain matrices for the three independent stress–strain coefficients (B_{11}, B_{12} and B_{44}) in the cubic lattice ($Fm\bar{3}m$) and the corresponding strain energy relations per unit volume at pressure P. Strain 1 is symmetry conserving but not volume conserving; strain 2 and 3 are nonsymmetry conserving but volume conserving.

	Stress–strain coefficient	Strain matrices	Strain energy
1.	B_{11}, B_{12}	$\begin{pmatrix} 1+\varepsilon & 0 & 0 \\ 0 & 1+\varepsilon & 0 \\ 0 & 0 & 1+\varepsilon \end{pmatrix}$	$u(\varepsilon, P) = -3P(\varepsilon + \varepsilon^2) + \frac{3}{2}(B_{11} + 2B_{12})\varepsilon^2$
2.	B_{11}, B_{12}	$\begin{pmatrix} 1+\varepsilon & 0 & 0 \\ 0 & 1+\varepsilon & 0 \\ 0 & 0 & \frac{1}{(1+\varepsilon)^2} \end{pmatrix}$	$u(\varepsilon) = 3(B_{11} - B_{12})\varepsilon^2$
3.	B_{44}	$\begin{pmatrix} 1 & \varepsilon & 0 \\ \varepsilon & 1 & 0 \\ 0 & 0 & \frac{1}{1-\varepsilon^2} \end{pmatrix}$	$u(\varepsilon) = 2B_{44}\varepsilon^2$

Table 2. Strain matrices for the nine independent stress–strain coefficients (B_{11}, B_{22}, B_{33}, B_{44}, B_{55}, B_{66}, B_{12}, B_{13} and B_{23}) in the orthorhombic lattice ($Pnma$) and the corresponding strain energy relations per unit volume at pressure P. Strain 1, 2 and 3 are symmetry conserving but not volume conserving; strain 4, 5 and 6 are volume conserving but not symmetry conserving; strain 7, 8 and 9 are both symmetry and volume conserving.

	Stress–strain coefficient	Strain matrices	Strain energy
1.	B_{11}	$\begin{pmatrix} 1+\varepsilon & 0 & 0 \\ 0 & 1 & 0 \\ 0 & 0 & 1 \end{pmatrix}$	$u(\varepsilon, P) = -P\varepsilon + \frac{1}{2}B_{11}\varepsilon^2$
2.	B_{22}	$\begin{pmatrix} 1 & 0 & 0 \\ 0 & 1+\varepsilon & 0 \\ 0 & 0 & 1 \end{pmatrix}$	$u(\varepsilon, P) = -P\varepsilon + \frac{1}{2}B_{22}\varepsilon^2$
3.	B_{33}	$\begin{pmatrix} 1 & 0 & 0 \\ 0 & 1 & 0 \\ 0 & 0 & 1+\varepsilon \end{pmatrix}$	$u(\varepsilon, P) = -P\varepsilon + \frac{1}{2}B_{33}\varepsilon^2$
4.	B_{44}	$\begin{pmatrix} \frac{1}{(1-\varepsilon^2)^{\frac{1}{3}}} & 0 & 0 \\ 0 & \frac{1}{(1-\varepsilon^2)^{\frac{1}{3}}} & \frac{\varepsilon}{(1-\varepsilon^2)^{\frac{1}{3}}} \\ 0 & \frac{\varepsilon}{(1-\varepsilon^2)^{\frac{1}{3}}} & \frac{1}{(1-\varepsilon^2)^{\frac{1}{3}}} \end{pmatrix}$	$u(\varepsilon) = 2B_{44}\varepsilon^2$
5.	B_{55}	$\begin{pmatrix} \frac{1}{(1-\varepsilon^2)^{\frac{1}{3}}} & 0 & \frac{\varepsilon}{(1-\varepsilon^2)^{\frac{1}{3}}} \\ 0 & \frac{1}{(1-\varepsilon^2)^{\frac{1}{3}}} & 0 \\ \frac{\varepsilon}{(1-\varepsilon^2)^{\frac{1}{3}}} & 0 & \frac{1}{(1-\varepsilon^2)^{\frac{1}{3}}} \end{pmatrix}$	$u(\varepsilon) = 2B_{55}\varepsilon^2$
6.	B_{66}	$\begin{pmatrix} \frac{1}{(1-\varepsilon^2)^{\frac{1}{3}}} & \frac{\varepsilon}{(1-\varepsilon^2)^{\frac{1}{3}}} & 0 \\ \frac{\varepsilon}{(1-\varepsilon^2)^{\frac{1}{3}}} & \frac{1}{(1-\varepsilon^2)^{\frac{1}{3}}} & 0 \\ 0 & 0 & \frac{1}{(1-\varepsilon^2)^{\frac{1}{3}}} \end{pmatrix}$	$u(\varepsilon) = 2B_{66}\varepsilon^2$
7.	B_{12}, B_{13}, B_{23}	$\begin{pmatrix} (1+\varepsilon)^{\frac{2}{3}} & 0 & 0 \\ 0 & (1+\varepsilon)^{-\frac{1}{3}} & 0 \\ 0 & 0 & (1+\varepsilon)^{-\frac{1}{3}} \end{pmatrix}$	$u(\varepsilon) = \frac{1}{18}(4B_{11} - 4B_{12} - 4B_{13} + B_{22} + B_{33} + 2B_{23})\varepsilon^2$
8.	B_{12}, B_{13}, B_{23}	$\begin{pmatrix} (1+\varepsilon)^{-\frac{1}{3}} & 0 & 0 \\ 0 & (1+\varepsilon)^{\frac{2}{3}} & 0 \\ 0 & 0 & (1+\varepsilon)^{-\frac{1}{3}} \end{pmatrix}$	$u(\varepsilon) = \frac{1}{18}(4B_{22} - 4B_{12} - 4B_{23} + B_{11} + B_{33} + 2B_{13})\varepsilon^2$
9.	B_{12}, B_{13}, B_{23}	$\begin{pmatrix} (1+\varepsilon)^{-\frac{1}{3}} & 0 & 0 \\ 0 & (1+\varepsilon)^{-\frac{1}{3}} & 0 \\ 0 & 0 & (1+\varepsilon)^{\frac{2}{3}} \end{pmatrix}$	$u(\varepsilon) = \frac{1}{18}(4B_{33} - 4B_{13} - 4B_{23} + B_{11} + B_{22} + 2B_{12})\varepsilon^2$

calculate $B_{ij}(P)$, the elastic moduli with respect to a shear-stress-free reference state at pressure P. The B_{ij} are often called the stress–strain coefficients, which are directly related to sound velocities at high pressure [28]. They are equal to C_{ij} when the pressure vanishes, as explained in detail in [27].

For CaF$_2$ under pressure, there are three, nine and five independent stress–strain coefficients in the cubic ($Fm\bar{3}m$),

orthorhombic ($Pnma$) and hexagonal ($P6_3/mmc$) phases, respectively. Tables 1–3 show the strain matrices ($\mathbf{1} + \boldsymbol{\varepsilon}$) and the corresponding strain energy relations per unit volume at pressure P in these three phases. Each strain was parameterized by a single variable ε and we calculated the total energy for a number of small values of ε. For these small distortions obtained from left-multiplying unit-cell-lattice matrices by these strain matrices, the calculated total
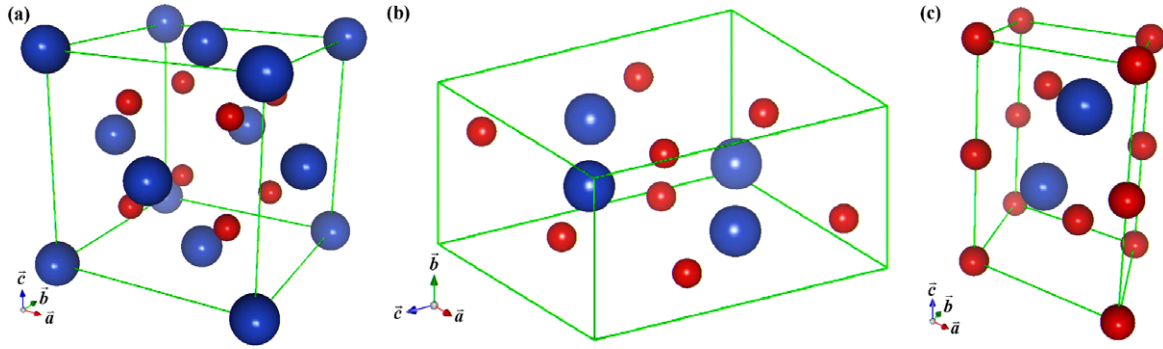
Figure 1. Conventional unit cells of (a) $Fm\bar{3}m$ cubic, (b) $Pnma$ orthorhombic and (c) $P6_3/mmc$ hexagonal structures. Small and large circles represent F and Ca atoms, respectively.

Table 3. Strain matrices for the five independent stress–strain coefficients (B_{11}, B_{12}, B_{13}, B_{33} and B_{44}) in the hexagonal lattice ($P6_3/mmc$) and the corresponding strain energy relations per unit volume at pressure P. Strain 1 and 5 are symmetry conserving but not volume conserving; strain 3 and 4 are volume conserving but not symmetry conserving; strain 2 is both symmetry and volume conserving.

	Stress–strain coefficient	Strain matrices	Strain energy
1.	B_{11}, B_{12} and B_{13}	$\begin{pmatrix} 1+\varepsilon & 0 & 0 \\ 0 & 1+\varepsilon & 0 \\ 0 & 0 & 1+\varepsilon \end{pmatrix}$	$u(\varepsilon, P) = -3P(\varepsilon + \varepsilon^2) + \frac{1}{2}(2B_{11} + 2B_{12} + 4B_{13} + B_{33})\varepsilon^2$
2.	B_{11}, B_{12} and B_{13}	$\begin{pmatrix} (1+\varepsilon)^{-\frac{1}{3}} & 0 & 0 \\ 0 & (1+\varepsilon)^{-\frac{1}{3}} & 0 \\ 0 & 0 & (1+\varepsilon)^{\frac{2}{3}} \end{pmatrix}$	$u(\varepsilon) = \frac{1}{9}(B_{11} + B_{12} - 4B_{13} + 2B_{33})\varepsilon^2$
3.	B_{11} and B_{12}	$\begin{pmatrix} \frac{1+\varepsilon}{(1-\varepsilon^2)^{\frac{1}{3}}} & 0 & 0 \\ 0 & \frac{1-\varepsilon}{(1-\varepsilon^2)^{\frac{1}{3}}} & 0 \\ 0 & 0 & \frac{1}{(1-\varepsilon^2)^{\frac{1}{3}}} \end{pmatrix}$	$u(\varepsilon) = (B_{11} - B_{12})\varepsilon^2$
4.	B_{44}	$\begin{pmatrix} \frac{1}{(1-\varepsilon^2)^{\frac{1}{3}}} & 0 & 0 \\ 0 & \frac{1}{(1-\varepsilon^2)^{\frac{1}{3}}} & \frac{\varepsilon}{(1-\varepsilon^2)^{\frac{1}{3}}} \\ 0 & \frac{\varepsilon}{(1-\varepsilon^2)^{\frac{1}{3}}} & \frac{1}{(1-\varepsilon^2)^{\frac{1}{3}}} \end{pmatrix}$	$u(\varepsilon) = 2B_{44}\varepsilon^2$
5.	B_{33}	$\begin{pmatrix} 1 & 0 & 0 \\ 0 & 1 & 0 \\ 0 & 0 & 1+\varepsilon \end{pmatrix}$	$u(\varepsilon, P) = -P\varepsilon + \frac{1}{2}B_{33}\varepsilon^2$

energies were fit to a polynomial in ε and then equated to the appropriate elastic coefficient expression. From all of the fits we obtained a system of linear equations for the elastic coefficients, which was solved for the B_{ij}.

3. Results and discussion

3.1. Crystal structures and pressure-induced phase transitions

We first performed an optimization of the geometry of the lattice and internal structural parameters. According to the literature mentioned above, the sequence of the pressure-induced phase transition of CaF$_2$ is the cubic fluorite structure ($Fm\bar{3}m$), the orthorhombic cotunnite PbCl$_2$-type structure ($Pnma$) and the hexagonal Ni$_2$In-type structure ($P6_3/mmc$). At these phase transformations, the coordination number of Ca increases from eight to nine and then to eleven. The atomic positions for the $Fm\bar{3}m$ phase are Ca (0, 0, 0) and F ($\pm 1/4$, $\pm 1/4$, $\pm 1/4$) and the lattice constant a_0 is 5.4630 Å [29, 30]. In the PbCl$_2$-type structure, the Ca, F1 and F2 ions are at (0.2539, 1/4, 0.1094), (0.8595, 1/4, 0.0731) and (0.4780, 1/4, 0.8344), respectively; the lattice

constants are $a_0 = 6.018$ Å, $b_0 = 3.614$ Å and $c_0 = 7.023$ Å [31]. In the Ni$_2$In-type structure, the Ca and the two F ions occupy the following positions, (1/3, 2/3, 1/4), (0, 0, 0) and (1/3, 2/3, 3/4), respectively. The Ni$_2$In-type structure can also be presented in an orthorhombic description using the space group $Pnma$ and the lattice parameters satisfy the following relations: $a_o = c_h$, $b_o = a_h$, $c_o = 3^{1/2}a_h$ and the atomic positions of Ca are (1/4, 1/4, 1/12) and of F are (1/4, 1/4, 5/12) and (0, 3/4, 1/4). Figure 1 shows the schematic crystal structures of these three phases.

Table 4 lists the theoretical lattice parameters (lattice constants and internal parameters) and bulk moduli of CaF$_2$ in three phases and also includes the available experimental results for comparison. For the $Fm\bar{3}m$ phase, the lattice constant $a_0 = 5.509$ Å and bulk modulus $B_0 = 79$ GPa are in good agreement with the experimental values of 5.4630 Å and 82 GPa, respectively. In the $Pnma$ case, both the lattice constants (a_0, b_0 and c_0) and the atomic positions of Ca and F ions agree well with the experimental data [31]. The $B_0 = 66$ GPa of the $Pnma$ phase is smaller than that of the $Fm\bar{3}m$ phase, unlike the calculations by Wu *et al* [16], which

Table 4. Lattice parameters, atomic positions and bulk moduli of three phases for CaF_2 at zero pressure.

	Lattice parameters (Å)		B_0 (GPa)	
	Theoretical	Experimental	Theoretical	Experimental
$Fm\bar{3}m$	$a_0 = 5.509$	$a_0 = 5.4630^a$	79	82.0 ± 0.7^b
$Pnma$	$a_0 = 6.020$	$a_0 = 6.018^c$	66	
	$b_0 = 3.660$	$b_0 = 3.614$		
	$c_0 = 7.108$	$c_0 = 7.023$		
	Ca (0.2526, 1/4, 0.1030)	Ca (0.2539, 1/4, 0.1094)		
	F1 (0.8595, 1/4, 0.0795)	F1 (0.8595, 1/4, 0.0731)		
	F2 (0.4880, 1/4, 0.8417)	F2 (0.4780, 1/4, 0.8344)		
$P6_3/mmc$	$a_0 = 3.873$		72	
	$c_0 = 5.844$			

^{a} Reference [29, 30]. ^{b} Reference [11]. ^{c} Reference [31].
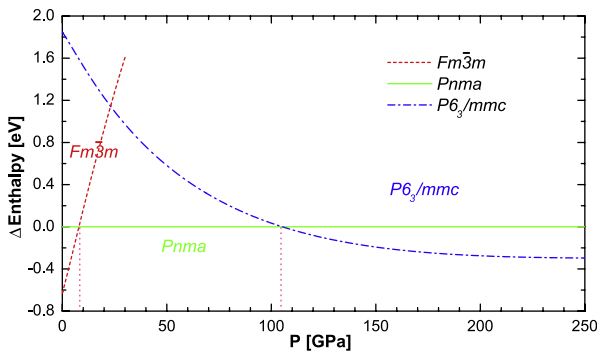

Figure 2. Variation with pressure of enthalpies $H = H(P)$ of CaF_2 phases relative to the enthalpy of the *Pnma* structure. Enthalpy is normalized per unit cell of the *Pnma* phase.
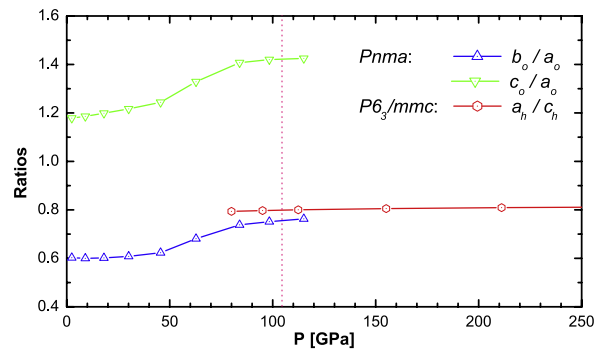

Figure 3. Variation of the c_o/a_o, b_o/a_o and a_h/c_h ratios with pressures in the *Pnma* and $P6_3/mmc$ phases. a_h/c_h corresponds to b_o/a_o when the $P6_3/mmc$ phase is presented using the space group *Pnma*.

shows that B_0 only present a slight change. Our optimized lattice constants ($a_0 = 3.873$ Å and $c_0 = 5.844$ Å) for the $P6_3/mmc$ case are comparable with another theoretical work ($a_0 = 3.8851$ Å and $c_0 = 5.9267$ Å) by Wu *et al* [16] and the ratio c_0/a_0 is found to be 1.51. In our calculations, the B_0 of the $P6_3/mmc$ phase is between the values of the $Fm\bar{3}m$ and *Pnma* phases.

In figure 2, enthalpies of the $Fm\bar{3}m$ and $P6_3/mmc$ structures relative to the enthalpy of the *Pnma* phase versus pressure are shown. By comparing the enthalpies $H = H(P)$ of the three structures we estimated the pressures at which phase transitions occur. The transition from $Fm\bar{3}m$ to *Pnma* occurs at around 8 GPa with a volume collapse of 8.4%, in very close agreement with the experimental results of 8.01 GPa and 8.3% [13]. According to our calculation, CaF_2 further transforms to the $P6_3/mmc$ structure at around 105 GPa, overestimating the experiment result of 84 GPa [17]. It is accompanied with a small volume decrease of 1.2%. Figure 3 shows the lattice-constant ratios for the *Pnma* and $P6_3/mmc$ phases of CaF_2 as a function of pressure. It is shown clearly that there is no remarkable increase of the a_h/c_h ratio in the hexagonal phase and the corresponding ratio of b_o/a_o in the orthorhombic structure increases with increasing pressure, especially after 50 GPa. At around 105 GPa, the transition pressure, the b_o/a_o ratio of 0.75 changes abruptly to the a_h/c_h ratio of 0.80.

3.2. Electronic properties

The self-consistent band structures for CaF_2 were obtained at ambient as well as at high pressures. Figure 4 shows the variation of the band gap with pressures in the cubic, orthorhombic and hexagonal phases. The calculated indirect gap (X → Γ) is 7.3 eV at zero pressure, which is much smaller than the experimental values (11.8 eV) [1]. It is due to the well-known reason that DFT-LDA (GGA) calculations underestimate the band gap by a factor of typically two. The band gap in the $Fm\bar{3}m$ phase and forepart region of the *Pnma* phase increases with increasing pressure and decreases from around 60 GPa in the *Pnma*-phase region, while there is a sudden gap collapse of 1.3 eV at the *Pnma*-to-$P6_3/mmc$ transition pressure, as shown in figure 4. At the $Fm\bar{3}m$-to-*Pnma* phase transition point, there is also a gap change, an increase of about 0.3 eV, being much smaller than that of the *Pnma*-to-$P6_3/mmc$ transition.

In order to analyze the electronic properties of CaF_2, we have also calculated the density of states (DOS). The total and partial DOS calculations show that the upper valence bands, which lie close to the Fermi level, are contributed by the p orbitals of F atoms, and the conduction bands mainly arise from the d states of Ca atoms. Figure 5 is the projected DOS onto $p_x + p_y$ and p_z orbitals of F2 atoms for the *Pnma* and $P6_3/mmc$ phases at different pressures. It is shown clearly that p_z states of F2 atoms are separate from p_x and p_y towards
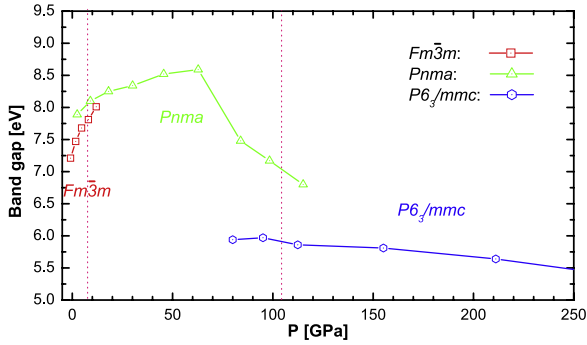
Figure 4. Calculated variation of the band gap with pressures in the $Fm\bar{3}m$, $Pnma$ and $P6_3/mmc$ phases within the GGA.
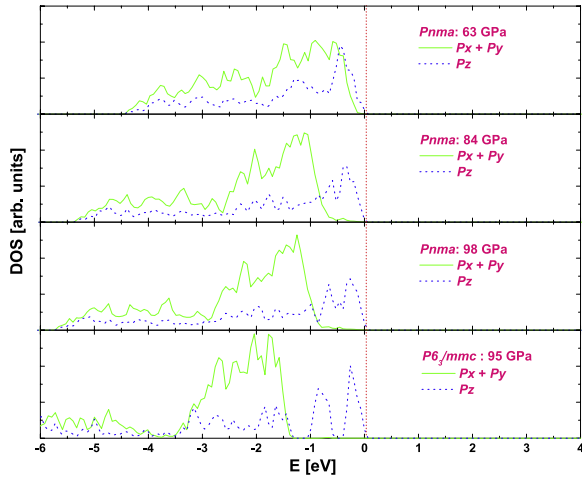

Figure 5. Projected DOS onto $p_x + p_y$ and p_z orbitals of F2 (defined in table 4) atoms for the $Pnma$ and $P6_3/mmc$ phases of CaF$_2$ at different pressures.

the Fermi level under high pressure (more than 60 GPa), which explains the decrease of band gap with increasing pressure in the $Pnma$ phase. Near the $Pnma$-to-$P6_3/mmc$ transition pressure, this p_z-separation in the $P6_3/mmc$ phase is more pronounced than that of in the $Pnma$ phase. According to our DOS calculations, there is no similar p_z-separation for F1 atom p states.

3.3. Elastic properties

We next consider how the crystal elastic moduli change with pressure. Firstly, by fitting the variation of total energy with volume to the Birch–Murnaghan equation of state, we obtained the bulk modulus of the $Fm\bar{3}m$, $Pnma$ and $P6_3/mmc$ phases as a function of pressure, as we can see figure 6. The bulk modulus at the $Fm\bar{3}m$-to-$Pnma$ transition pressure changes abruptly from 113 to 99 GPa, with a bulk modulus decrease of 14 GPa, and at the $Pnma$-to-$P6_3/mmc$ transition point, the bulk modulus increases from 446 GPa for the $Pnma$ phase to 462 GPa for the $P6_3/mmc$ phase.

Further research on the elastic properties of CaF$_2$ are calculations on $B_{ij}(P)$, the stress–strain coefficients, being directly related to sound velocities at high pressure. Figure 7
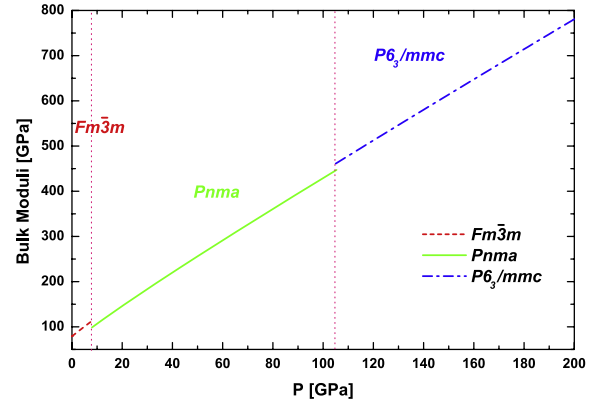

Figure 6. Bulk moduli of $Fm\bar{3}m$, $Pnma$ and $P6_3/mmc$ as a function of pressure. These bulk moduli are based on the Birch–Murnaghan equation of state.

shows the variation with pressure of the stress coefficients B_{ij} for the $Fm\bar{3}m$, $Pnma$ and $P6_3/mmc$ phases. Our calculations demonstrated that the B_{ij} satisfy the requirement of mechanical stability in the cubic, orthorhombic and hexagonal crystals. The stability conditions lead to the following restrictions on the elastic moduli: for the cubic lattice, $B_{11} > 0$, $B_{44} > 0$ and $B_{11}^2 > B_{11}(B_{11} + B_{12})/2 > B_{12}^2$; for the orthorhombic lattice, $B_{ii} > 0$ $(i = 1, 2, \ldots, 6)$, $B_{ii}B_{jj} > B_{ij}^2$ $(i \neq j = 1, 2, 3)$ and $B_{33}(B_{11}B_{12} - B_{12}^2)^2 > B_{23}^2 B_{11} + B_{13}^2 B_{22} - 2B_{12}B_{13}B_{23}$; and for the hexagonal lattice, $B_{33} > 0$, $B_{44} > 0$ and $B_{11}B_{33} > B_{33}(B_{11}+B_{12})/2 > B_{13}^2$ [32].

At ambient pressure, CaF$_2$ is cubic $Fm\bar{3}m$ structure with $C_{11} = 162.8$ GPa, $C_{12} = 45.6$ GPa and $C_{44} = 31.7$ GPa, being in good agreement with the experimental values of 164.2 GPa, 44 GPa and 33.7 GPa, respectively [33]. In the orthorhombic lattice, B_{11}, B_{22} and B_{33} denote the elastic properties along the X, Y and Z directions, corresponding to B_{11} in the cubic crystal. From figure 7(b), we can see that B_{33} is larger than B_{11} and B_{22} under lower pressure, indicating a more remarkable elasticity in the Z axis than that in the X and Y directions, and B_{11} is separated from B_{22} and B_{33} with increasing pressure. In the cubic lattice, B_{11}, representing the elasticity along the X (or Y or Z) direction, is 200 GPa and comparable with B_{11} (180 GPa), B_{22} (172 GPa) and B_{33} (214 GPa) of the $Pnma$ phase at the $Fm\bar{3}m$-to-$Pnma$ transition point. It is shown clearly that there are changes of elasticity in a certain direction when the $Fm\bar{3}m$ phase transforms to the $Pnma$ phase. On the other hand, B_{44}, B_{55} and B_{66} in the orthorhombic structure indicate the shear elasticity applied to the two-dimensional rectangle lattice, such as in the (100), (010) and (001) planes. According to our calculations, B_{44} and B_{55} increase with increasing pressure, but B_{66} does not increase under high pressures. B_{44} in the cubic phase at 8 GPa of the $Fm\bar{3}m$-to-$Pnma$ transition pressure equals 37.2 GPa and is smaller than B_{44} (40 GPa), B_{55} (50.5 GPa) and B_{66} (74.6 GPa) in the $Pnma$ phase. It implies shear transformations in the $Pnma$ phase are more difficult than in the cubic phase in CaF$_2$.

For the hexagonal case, B_{11} and B_{33} have close values, suggesting the longitudinal elasticities of the a_h and c_h vectors being similar. It is in accordance with the fact that the ratio
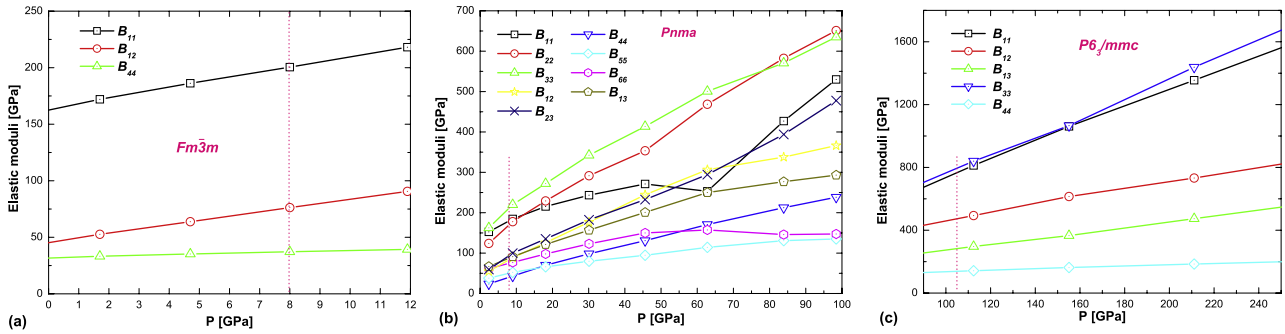
Figure 7. The elastic moduli (specifically, the stress–strain coefficients) of the $Fm\bar{3}m$, $Pnma$ and $P6_3/mmc$ phases as a function of pressure. In the $Fm\bar{3}m$, $Pnma$ and $P6_3/mmc$ phases, there are three, nine and five independent elastic moduli (stress–strain coefficients), respectively. Pink dot lines indicate the phase transition pressures.

a_h/c_h is almost a constant, as we can see in figures 3 and 7(c). As mentioned before, because the lattice vector a_o of the orthorhombic phase corresponds the c_h vector of the hexagonal phase, we compared $B_{11}^{(o)}$ in the orthorhombic lattice with $B_{33}^{(h)}$ in the hexagonal case. Both elastic moduli actually denote the longitudinal elasticity of the same lattice vector. At the $Pnma$-to-$P6_3/mmc$ transition pressure of 105 GPa, $B_{11}^{(o)}$ and $B_{33}^{(h)}$ are 572 GPa and 800 GPa, respectively. $B_{11}^{(o)}$ is much smaller than $B_{33}^{(h)}$. It is shown clearly that the longitudinal elasticity along the c_h (or a_o) vector has a sudden increase at the transition point and the compressibility along the c_h (or a_o) direction for the orthorhombic phase is stronger than that in the hexagonal case. Similarly, we compared $B_{22}^{(o)}$ with $B_{11}^{(h)}$ because of the relation between b_o and a_h. According to our calculations, at the transition pressure, $B_{22}^{(o)}$ of 682 GPa is smaller than $B_{11}^{(h)}$ of 767 GPa, also indicating a stronger longitudinal compressibility than that in the hexagonal phase. From the DOS calculations for the $P6_3/mmc$ phase (see figure 5), we can conclude that the p_z-orbitals are more delocalized, suggesting more pronounced electron overlaps and repulsions between the neighbor F atoms, which is in accordance with the fact that a sudden change of incompressibility occurs at the transition point.

4. Conclusions

We have calculated structural, electronic and elastic properties of CaF$_2$ for different phases in the framework of DFT using the GGA. In conclusion, our calculated structural parameters for the $Fm\bar{3}m$ and $Pnma$ phases are in good agreement with experimental data. The structural calculations also demonstrate that the phase transition of CaF$_2$ from the fluorite structure ($Fm\bar{3}m$) to the orthorhombic cotunnite-type structure ($Pnma$) occurs at 8 GPa, in good agreement with experimental data, and the further transformation from the orthorhombic phase to the hexagonal Ni$_2$In-type ($P6_3/mmc$) structure occurs at about 105 GPa, overestimating the transition pressure with respect to the experiment. Our calculations have shown that the band gap of CaF$_2$ increases with increasing pressure up to 60 GPa. However, for the hexagonal and hindpart orthorhombic phases, the band gap decreases with increasing pressure, which is due to the p_z-state shift towards the Fermi level.

Our calculated elastic constants for the cubic phase at ambient pressure agree well with the experimental values. The stress–strain coefficients calculations show that shear transformations in the $Pnma$ phase are more difficult than in the cubic phase in CaF$_2$ and the compressibility along the c_h (or a_o) direction for the orthorhombic phase is stronger than that in the hexagonal case, which is due to the delocalization of p_z-electrons.

References

[1] Rubloff G W 1971 *Phys. Rev.* B **5** 662
[2] Barth J, Johnson R L, Cardona M, Fuchs D and Bradshaw A M 1990 *Phys. Rev.* B **41** 3291
[3] Gan F, Xu Y N, Huang M Z, Ching W Y and Harrison J G 1992 *Phys. Rev.* B **45** 8248
[4] Verstraete M and Gonze X 2003 *Phys. Rev.* B **68** 195123
[5] Shi H, Eglitis R I and Borstel G 2005 *Phys. Rev.* B **72** 045109
[6] Anderson O L 1995 *Equation of State of Solids for Geophysics and Ceramic Science* (Oxford: Oxford University Press)
[7] Seifert K F and Bunsenges B 1966 *Phys. Chem.* **70** 1041
[8] Dandekar D P and Jamieson J C 1969 *Trans. Am. Crystallogr. Assoc.* **5** 19
[9] Gerward L, Olsen J S, Steenstrup S, Åsbrink S and Waskowska A 1992 *J. Appl. Crystallogr.* **25** 578
[10] Burnett J H, Levine Z H and Shirley E L 2001 *Phys. Rev.* B **64** 241102(R)
[11] Speziale S and Duffy T S 2002 *Phys. Chem. Miner.* **29** 465
[12] Kanchana V, Vaitheeswaran G and Rajagopalan M 2003 *Physica* B **328** 283
[13] El'kin F S, Tsiok O B, Khvostantsev L G and Brazhkin V V 2005 *J. Exp. Theor. Phys.* **100** 971
[14] Khenata R, Daoudi B, Sahnoun M, Baltache H, Rérat M, Reshak A H, Bouhafs B, Abid H and Driz M 2005 *Eur. Phys. J.* B **47** 63
[15] Pendás A M, Recio J M, Flórez M and Luaña V 1994 *Phys. Rev.* B **49** 5858
[16] Wu X, Qin S and Wu Z Y 2006 *Phys. Rev.* B **73** 134103

[17] Dorfman S M, Jiang F, Mao Z, Kubo A, Prakapenka V and Duffy T S 2007 *American Geophysical Union, Fall Mtg 2007*
[18] Catti M, Dovesi R, Pavese A and Saunders V R 1991 *J. Phys.: Condens. Matter* **3** 4151
[19] Shirley E L 1998 *Phys. Rev.* B **58** 9579
[20] Benedict L X and Shirley E L 1999 *Phys. Rev.* B **59** 5441
[21] Dubrovinsky L S, Saxena S K, Lazor P, Ahuja R, Eriksson O, Wills J M and Johansson B 1997 *Nature* **388** 362
[22] Blöchl P E 1994 *Phys. Rev.* B **50** 17953
[23] Kresse G and Furthmüller J 1996 *Phys. Rev.* B **54** 11169
[24] Kresse G and Joubert D 1999 *Phys. Rev.* B **59** 1758
[25] Perdew J P, Chevary J A, Vosko S H, Jackson K A, Pederson M R, Singh D J and Fiolhais C 1992 *Phys. Rev.* B **46** 6671
[26] Perdew J P, Chevary J A, Vosko S H, Jackson K A, Pederson M R, Singh D J and Fiolhais C 1993 *Phys. Rev.* B **48** 4978
[27] Wallace D C 1972 *Thermodynamics of Crystals* (New York: Wiley)
[28] Lee B 2008 *Phys. Rev.* B **77** 134105
[29] Smakula A and Kalnajs J 1955 *Phys. Rev.* **99** 1731
[30] Wu X, Wu Z Y, Guo L, Liu C, Liu J and Li X D 2005 *Solid State Commun.* **135** 780
[31] Morris E, Groy T and Leinenweber K 2001 *J. Phys. Chem. Solids* **62** 1117
[32] Winternheimer C G and McCurdy A K 1978 *Phys. Rev.* B **18** 6576
[33] 2003 http://www.corning.com/docs/specialtymaterials/pisheets/H0607_CaF2_Product_Sheet.pdf